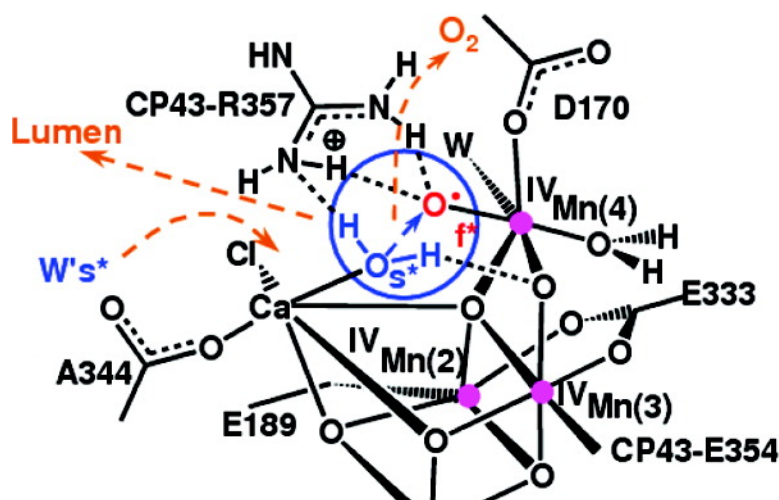Article

Quantum Mechanics/Molecular Mechanics Study of the Catalytic Cycle of Water Splitting in Photosystem II

Eduardo M. Sproviero, Jos A. Gascn, James P. McEvoy, Gary W. Brudvig, and Victor S. Batista

More About This Article

Additional resources and features associated with this article are available within the HTML version:

- Supporting Information
- Links to the 7 articles that cite this article, as of the time of this article download
- Access to high resolution figures
- Links to articles and content related to this article
- Copyright permission to reproduce figures and/or text from this article

View the Full Text HTML

Quantum Mechanics/Molecular Mechanics Study of the Catalytic Cycle of Water Splitting in Photosystem II

Eduardo M. Sproviero, José A. Gascón,[†] James P. McEvoy,[‡] Gary W. Brudvig, and Victor S. Batista*

Department of Chemistry, Yale University, P.O. Box 208107, New Haven, Connecticut 06520-8107

Received August 14, 2007; E-mail: victor.batista@yale.edu

Abstract: This paper investigates the mechanism of water splitting in photosystem II (PSII) as described by chemically sensible models of the oxygen-evolving complex (OEC) in the S_0-S_4 states. The reaction is the paradigm for engineering direct solar fuel production systems since it is driven by solar light and the catalyst involves inexpensive and abundant metals (calcium and manganese). Molecular models of the OEC Mn_3CaO_4Mn catalytic cluster are constructed by explicitly considering the perturbational influence of the surrounding protein environment according to state-of-the-art quantum mechanics/molecular mechanics (QM/MM) hybrid methods, in conjunction with the X-ray diffraction (XRD) structure of PSII from the cyanobacterium *Thermosynechococcus elongatus*. The resulting models are validated through direct comparisons with high-resolution extended X-ray absorption fine structure spectroscopic data. Structures of the S_3, S_4, and S_0 states include an additional μ-oxo bridge between Mn(3) and Mn(4), not present in XRD structures, found to be essential for the deprotonation of substrate water molecules. The structures of reaction intermediates suggest a detailed mechanism of dioxygen evolution based on changes in oxidization and protonation states and structural rearrangements of the oxomanganese cluster and surrounding water molecules. The catalytic reaction is consistent with substrate water molecules coordinated as terminal ligands to Mn(4) and calcium and requires the formation of an oxyl radical by deprotonation of the substrate water molecule ligated to Mn(4) and the accumulation of four oxidizing equivalents. The oxyl radical is susceptible to nucleophilic attack by a substrate water molecule initially coordinated to calcium and activated by two basic species, including CP43-R357 and the μ-oxo bridge between Mn(3) and Mn(4). The reaction is concerted with water ligand exchange, swapping the activated water by a water molecule in the second coordination shell of calcium.

1. Introduction

Photosynthesis couples O_2 evolution with the fixation of CO_2, sustaining life on earth by generating an aerobic atmosphere and providing a carbon source for biosynthesis. Central to this process is photosystem II (PSII), a transmembrane protein complex found in the thylakoid membrane of green-plant chloroplasts and the internal membranes of cyanobacteria. The PSII complex includes more than 20 protein subunits, a photon-antenna system of chlorophyll pigments, and multiple electron-transfer quinone cofactors (see Figure 1). The complex harvests solar light and drives the reduction and protonation of plastoquinone (PQ), using electrons produced by water oxidation at the oxygen-evolving complex (OEC) and protons from the stroma. The overall reaction generates a pH gradient across the membrane that is necessary for ATP biosynthesis.

In contrast to both chemical and electrochemical water splitting, photosynthetic water oxidation proceeds with very little

driving force and requires only moderate activation energies.[1−5] Moreover, the OEC turns over rapidly with up to 50 molecules of O_2 released per second, despite having to protect itself from photochemical oxidative damage. The catalytic reaction is the paradigm for engineering direct solar fuel production systems since it is driven by solar light and involves a catalyst based on inexpensive and abundant metals (calcium and manganese).

Our current understanding of photosynthetic water oxidation is based on the catalytic cycle proposed by Joliot and Kok (see Figure 2),[6,7] establishing the foundation for further studies on the chemical nature of reaction intermediates and electronic state transitions responsible for the accumulation of oxidizing equivalents.[8−12] Extensive research over many years established that each transition in the catalytic cycle comprises the photo-

† Current address: Department of Chemistry, University of Connecticut, Storrs, CT 06269-3060.

‡ Current address: Department of Chemistry, Regis University, Denver, CO 80221.

(1) Diner, B. A.; Babcock, G. T. *Oxygenic Photosynthesis: The Light Reactions*; Kluwer Academic Publishers: Dordrecht, The Netherlands, 1996.
(2) Debus, R. J. *Biochim. Biophys. Acta* **1992**, *1102*, 269−352.
(3) Witt, H. T. *Ber. Bunsen-Ges. Phys. Chem.* **1996**, *100*, 1923−1942.
(4) Britt, R. D. *Oxygenic Photosynthesis: The Light Reactions*; Kluwer Academic Publishers: Dordrecht, The Netherlands, 1996.
(5) McEvoy, J. P.; Brudvig, G. W. *Chem. Rev.* **2006**, *106*, 4455−4483.
(6) Joliot, P.; Barbieri, G.; Chabaud, R. *Photochem. Photobiol.* **1969**, *10*, 309−329.
(7) Kok, B.; Forbush, B.; McGloin, M. *Photochem. Photobiol.* **1970**, *11*, 457−475.
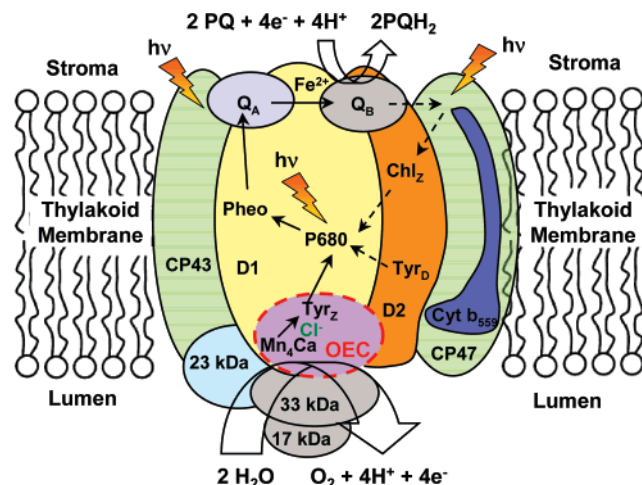
Figure 1. PSII complex and its antenna system, consisting of more than 20 protein subunits, either embedded in the thylakoid membrane or associated with its lumenal surface. Light energy is trapped predominantly by the outer antenna and transferred to the photochemically active reaction centers, via chlorophyll-binding proteins CP47 and CP43, where it is used to drive the water-splitting reaction at the OEC. The electrons extracted from water are passed from the lumenally located Ca/Mn cluster to P680$^+$ via D1-Y 161 (Tyr$_Z$), a process that is coupled to electron transfer (ET) from P680 to pheophytin (Pheo), Q_A, and onto Q_B, defining the ET pathway marked by the solid arrows. Broken arrows indicate secondary ET pathways, which may play a photoprotective role. The protons and molecular oxygen produced during the water-splitting reaction are released into the lumen.
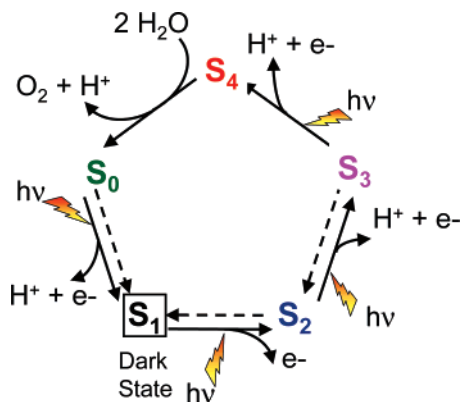

Figure 2. Catalytic cycle of photosynthetic water oxidation proposed by Joliot and Kok.[6,7] Dotted arrows describe reactions that relax the system back to the dark stable state S_1 within minutes.

oxidation of the chlorophyll *a* species P680, forming the chlorophyll cation radical P680$^{•+}$ by ultrafast electron transfer to pheophytin (Pheo), quinone cofactor (Q_A), and the subsequent reduction of PQ at the Q_B site. The oxidized chlorophyll species P680$^{•+}$ is reduced by abstraction of an electron from the OEC, a process mediated by the redox-active tyrosine residue, Y_Z (D1-Tyr161).[13,14] Successive photoinduced electron-abstraction events

advance the OEC from the S_0 to the S_4 state,[7] increasingly oxidizing the oxomanganese complex. The most oxidized state (S_4) spontaneously decays (without additional light) into the S_0 state, forming molecular dioxygen.

In recent work,[9] we have proposed structural models of the S_0, S_1, and S_2 states of the OEC in PSII, found to be partially consistent with available mechanistic data and also compatible with X-ray diffraction (XRD) models[15] and extended X-ray absorption fine structure (EXAFS) measurements.[16,17] The models were developed according to state-of-the-art quantum mechanics/molecular mechanics (QM/MM) hybrid methods, explicitly including the influence of the surrounding protein environment on the coordination of water molecules to the OEC, the protonation states of the ligands, and the oxidation states of metal centers stabilized by the proteinaceous ligation scheme. However, QM/MM structural models of the S_3 and S_4 states have yet to be reported and are the subject of this paper. In addition, this paper analyzes the complete set of electronic state transitions suggested by the QM/MM structural models of the OEC in the S_0–S_4 states with complete ligation by the protein, water, and chloride. The resulting OEC catalytic intermediates are validated through direct comparisons between calculated and experimental EXAFS spectra.[16–19]

The paper is organized as follows. Section 2 describes the preparation of QM/MM structural models, the QM/MM methodology, and the methods applied for simulations of EXAFS spectra. Section 3 presents the resulting QM/MM structural models of the S_0–S_4 intermediates along the catalytic cycle, including a detailed description of the structural rearrangements in the oxomanganese cluster, rearrangements of water molecules around the OEC, changes in the oxidization states of specific metal centers, and the protonation states of the OEC ligands. Section 3 also presents a discussion of the proton exit channel to the lumen, the water-channel pathways, the direct comparisons between calculated and experimental EXAFS spectra, and a discussion of the resulting QM/MM catalytic cycle as compared to previous proposals, including mechanisms based on experimental work,[8,11,20–26] and studies of inorganic model complexes isolated from the influence of the surrounding protein environment.[27,28] Section 4 summarizes and concludes.

(8) McEvoy, J. P.; Gascón, J. A.; Sproviero, E. M.; Batista, V. S.; Brudvig, G. W. *Photosynthesis: Fundamental Aspects to Global Perspectives*; Allen Press, Inc.: Lawrence, KS, 2005; Vol. 1.
(9) Sproviero, E. M.; McEvoy, J. P.; Gascón, J. A.; Brudvig, G. W.; Batista, V. S. *J. Chem. Theory Comput.* **2006**, *4*, 1119−1134.
(10) Sproviero, E. M.; Gascón, J. A.; McEvoy, J. P.; Brudvig, G. W.; Batista, V. S. *Curr. Opin. Struct. Biol.* **2007**, *17*, 173−180.
(11) McEvoy, J. P.; Gascón, J. A.; Batista, V. S.; Brudvig, G. W. *Photochem. Photobiol.* **2005**, *4*, 940−949.
(12) Sproviero, E. M.; Shinopolous, K.; Gascón, J. A.; McEvoy, J.; Brudvig, G. W.; Batista, V. S. *Phil Trans. R. Soc. London, Ser. B* **2008**, *363*, 1149−1156.
(13) Debus, R. J.; Barry, B. A.; Sithole, I.; Babcock, G. T.; McIntosh, L. *Biochemistry* **1988**, *27*, 9071−9074.
(14) Metz, J. G.; Nixon, P. J.; Rogner, M.; Brudvig, G. W.; Diner, B. A. *Biochemistry* **1989**, *28*, 6960−6969.
(15) Ferreira, K. N.; Iverson, T. M.; Maghlaoui, K.; Barber, J.; Iwata, S. *Science* **2004**, *303*, 1831−1838.
(16) Dau, H.; Liebisch, P.; Haumann, M. *Phys. Chem. Chem. Phys.* **2004**, *6*, 4781−4792.
(17) Haumann, M.; Muller, C.; Liebisch, P.; Iuzzolino, L.; Dittmer, J.; Grabolle, M.; Neisius, T.; Meyer-Klaucke, W.; Dau, H. *Biochemistry* **2005**, *4*, 1894−1908.
(18) Dau H., private communication.
(19) Yano, J.; Pushkar, Y.; Glatzel, P.; Lewis, A.; Sauer, K.; Messinger, J.; Bergmann, U.; Yachandra, V. *J. Am. Chem. Soc.* **2005**, *127*, 14974−14975.
(20) Messinger, J. *Phys. Chem. Chem. Phys.* **2004**, *6*, 4764−4771.
(21) Vrettos, J. S.; Limburg, J.; Brudvig, G. W. *Biochim. Biophys. Acta* **2001**, *1503*, 229−245.
(22) McEvoy, J. P.; Brudvig, G. W. *Phys. Chem. Chem. Phys.* **2004**, *6*, 4754−4763.
(23) Robblee, J. H.; Cinco, R. M.; Yachandra, V. K. *Biochim. Biophys. Acta* **2001**, *1503*, 7−23.
(24) Pecoraro, V. L.; Baldwin, M. J.; Caudle, M. T.; Hsieh, W. Y.; Law, N. A. *Pure Appl. Chem.* **1998**, *70*, 925−929.
(25) Barber, J.; Ferreira, K. N.; Maghlaoui, K.; Iwata, S. *Phys. Chem. Chem. Phys.* **2004**, *6*, 4737−4742.
(26) Britt, R. D.; Campbell, K. A.; Peloquin, J. M.; Gilchrist, M. L.; Aznar, C. P.; Dicus, M. M.; Robblee, J.; Messinger, J. *Biochim. Biophys. Acta* **2004**, *1655*, 158−171.
(27) Lundberg, M.; Siegbahn, P. E. M. *Phys. Chem. Chem. Phys.* **2004**, *6*, 4772−4780.
(28) Siegbahn, P. E. M.; Lundberg, M. *Photochem. Photobiol.* **2005**, *4*, 1035−1043.

2. Methodology

2.1. QM/MM Structural Models. The QM/MM structural models reported in this paper are based on the London X-ray crystal structure of PSII from the cyanobacterium *Thermosynechococcus elongatus* (pdb access code 1S5L), reported at 3.5 Å resolution.[15] The model includes bridging oxides in the Mn_4Ca cluster and is largely consistent with subsequently developed X-ray structures at 3.2−3.0 Å resolution,[29,30] resolving nearly all amino acid residues and cofactors. The Berlin structure, at 3.0 Å resolution, provides a more complete description of the protein complex than the London structure, including an additional protein subunit, but a more incomplete description of the metal cluster (e.g., does not include bridging oxides between metal centers). Its higher resolution narrows the distance error for the protein and cofactor structures, but because of radiation damage to the OEC, the resolution of the OEC is significantly lower than the overall resolution of the X-ray crystal.[31] Therefore, there is no compelling reason to favor the Berlin structure over the London structure with regards to the description of the OEC. Both crystal models suffer from problems with radiation damage and have comparable moderate resolution in the description of the Mn_4Ca cluster. The key point is that the spectroscopic data are of much higher resolution and the computational structural models allow refinement to match the spectroscopic data.

Following previous work,[8−12] the computational models consider 1987 atoms of PSII including the Mn_3CaO_4Mn complex and all amino acid residues with α-carbons within 15 Å from any atom in the OEC metal cluster. The coordination of the Mn ions is completed by hydration, roughly consistent with pulsed electron paramagnetic resonance (EPR) experiments revealing the presence of several exchangeable deuterons near the Mn cluster in the S_0, S_1, and S_2 states.[26] Two of the ligated waters bound to Ca^{2+} and Mn(4) are considered to be substrate water molecules responsible for O=O bond formation in the $S_4 \rightarrow S_0$ transition.[8−12] The coordination of Ca^{2+} is satisfied with seven or eight ligands, as defined by the resulting geometry optimization of the Mn_3CaO_4Mn unit including bound water molecules, the proteinaceous ligation, and negative counterions. These fully relaxed QM/MM configurations are biologically meaningful since temperature effects on the PSII structure, protonation state, or charge localization are negligible, as recently reported by studies of X-ray absorption at 20 K and room temperature.[17]

Starting with the recently reported structural model of the S_1 state,[9] catalytic intermediate models of the S_0, S_2, S_3, and S_4 states are built by QM/MM geometry optimization after advancing the oxidation state of the oxomanganese complex. Transitions $S_0 \rightarrow S_1$, $S_2 \rightarrow S_3$, $S_3 \rightarrow S_4$, and $S_4 \rightarrow S_0$ are assumed to involve deprotonation of the cluster as indicated by experiments.[32] The structures of the resulting S-state reaction intermediates are partially validated by direct comparisons between calculated and experimental high-resolution EXAFS spectra. Calculations of complete free energy profiles that would allow for comparisons with kinetics experiments are beyond the scope of this paper and will be presented in future work.

Electronic States. For each catalytic intermediate, an exhaustive analysis of electronic states and relaxed nuclear configurations of the complex was performed for various possible initial-guess spin-electronic states. Calculations were based on the broken symmetry (BS) density functional theory (DFT) method,[33,34] since the complexes of interest have unpaired spins and therefore require spin-polarized calculations. The purity of the initial guess was found to be preserved whenever the spin state was consistent with the geometry of the Mn_3CaO_4Mn complex and the specific ligation/protonation scheme. Otherwise, the optimization process changed the electronic state to the ground state consistent with the corresponding nuclear configuration. Fully relaxed configurations were assessed not only in terms of the total energy of the system but also on the basis of structural and electronic properties as directly compared to magnetic experimental data.

2.2. QM/MM Methodology. Computational Implementation. The two-layer ONIOM electronic-embedding (EE) link-hydrogen atom approach,[35] implemented in *Gaussian 03*,[36] has been applied as in previous studies.[9,10,12,37−40] The preparation of the initial electronic state has been based on high-quality spin-electronic states for the ligated cluster of Mn ions, according to ligand field theory[41] as implemented in *Jaguar 5.5*.[42] Such a combined methodology has allowed for an exhaustive exploration of a variety of initial spin-electronic states, defined by the specific oxidation states for Mn centers. In addition, the approach exploits the computational capabilities of ONIOM, including both the link-hydrogen atom scheme for efficient and flexible definitions of QM layers and the possibility of modeling open-shell systems by performing unrestricted-DFT (e.g., UB3LYP) calculations.

QM/MM Boundary. The QM layer of ONIOM-EE QM/MM calculations is defined according to a reduced molecular domain that includes the Mn_3CaO_4Mn complex, the directly ligating carboxylate groups of E189, CP43-E354, A344, E333, D170, and D342, and the imidazole ring of H332[43] as well as bound water molecules and hydroxide and chloride ions (see Figure 3). The rest of the system defines the MM layer and is described by the Amber MM force field.[44] QM/MM boundaries are defined for the corresponding amino acid residues (i.e., E189, CP43-E354, A344, E333, D170, D342, and H332) by completing the covalency of frontier atoms.

Polarization Effects. The total energy E of the system is computed as follows:

$$E = E^{MM,full} + E^{QM,red} - E^{MM,red} \tag{1}$$

where $E^{MM,full}$ is the energy of the complete system as described by the Amber MM force field[44] while $E^{QM,red}$ and $E^{MM,red}$ are the energies of the reduced system computed at the QM and MM levels of theory, respectively. Electrostatic interactions between the reduced system and the surrounding protein are included in the evaluation of $E^{QM,red}$ and $E^{MM,red}$ at the QM and MM levels, respectively. Therefore, the resulting QM/MM evaluation of the total energy E involves a quantum mechanical description of polarization of the reduced system due to the electrostatic influence of the surrounding protein environment. The polarization of the protein environment, usually neglected in standard QM/MM calculations, is modeled according to the self-consistent "moving domain-QM/MM" approach.[9,39]

Basis Sets. A combination of basis sets is applied in order to optimize the efficiency of QM/MM calculations. The lacvp basis set for Mn ions considers nonrelativistic electron−core potentials, the 6-31G(2df)

(29) Biesiadka, J.; Loll, B.; Kern, J.; Irrgang, K. D.; Zouni, A. *Phys. Chem. Chem. Phys.* **2004**, *6*, 4733−4736.
(30) Loll, B.; Kern, J.; Saenger, W.; Zouni, A.; Biesiadka, J. *Nature* **2005**, *438*, 1040−1044.
(31) Yano, J.; Kern, J.; Irrgang, K.; Latimer, M. J.; Bergmann, U.; Glatzel, P.; Pushkar, Y.; Biesiadka, J.; Loll, B.; Sauer, K.; Messinger, J.; Zouni, A.; Yachandra, V. K. *Proc. Natl. Acad. Sci. U.S.A.* **2005**, *102*, 12047−12052.
(32) Lavergne, J.; Junge, W. *Photosynth. Res.* **1993**, *38*, 279−296.
(33) Noodleman, L. *J. Chem. Phys.* **1981**, *74*, 5737−5743.
(34) Noodleman, L.; Davidson, E. R. *Chem. Phys.* **1981**, *109*, 131−143.
(35) Dapprich, S.; Komaromi, K.; Byun, K.; Morokuma, K.; Frisch, M. *J. Mol. Str.* (*THEOCHEM*) **1999**, *461*, 1−21.
(36) Frisch, M. J. et al. *Gaussian 03*, revision A1; Gaussian, Inc.: Pittsburgh, PA, 2003.
(37) Gascón, J. A.; Batista, V. S. *Biophys. J.* **2004**, *87*, 2931−2941.
(38) Gascón, J. A.; Sproviero, E. M.; Batista, V. S. *J. Chem. Theory Comput.* **2005**, *1*, 674−685.
(39) Gascón, J. A.; Leung, S. S. F.; Batista, E. R.; Batista, V. S. *J. Chem. Theory Comput.* **2006**, *2*, 175−186.
(40) Gascón, J. A.; Sproviero, E. M.; Batista, V. S. *Acc. Chem. Res.* **2005**, *39*, 184−193.
(41) Vacek, G.; Perry, J. K.; Langlois, J. M. *Chem. Phys. Lett.* **1999**, *310*, 189−194.
(42) *Jaguar 5.5*; Schroedinger, LLC: Portland, OR, 1991−2003.
(43) Note that all amino acid residues are from the D1 protein subunit, unless otherwise indicated.
(44) Cornell, W. D.; Cieplak, P.; Bayly, C. I.; Gould, I. R.; Merz, K. M.; Ferguson, D. M.; Spellmeyer, D. C.; Fox, T.; Caldwell, J. W.; Kollman, P. A. *J. Am. Chem. Soc.* **1995**, *117*, 5179−5197.
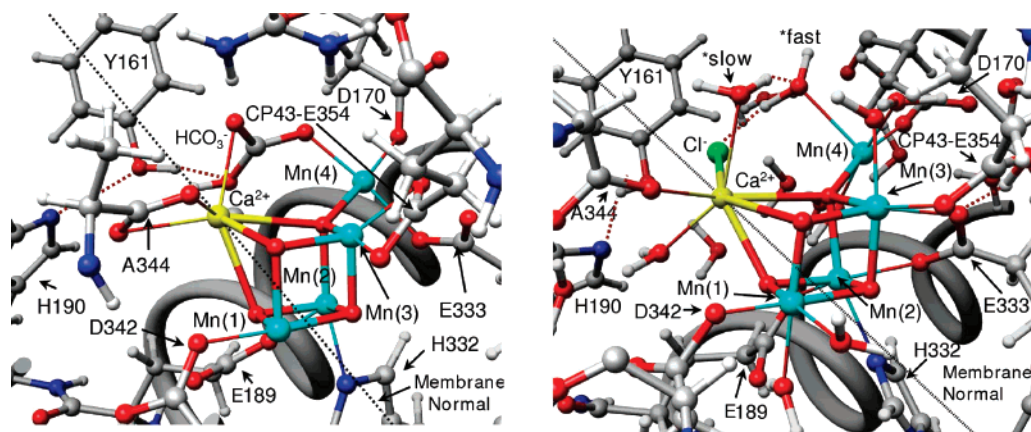
Figure 3. Comparison of molecular structures of the OEC of PSII in the S_1 state, as described by the 1S5L X-ray structure (left)[15] and a recently reported QM/MM model (right).[9] Substrate waters are labeled *slow and *fast (see text for explanation). All amino acid residues are labeled with one-letter symbols and correspond to the D1 protein subunit, unless otherwise indicated.

basis set for bridging O^{2-} ions includes polarization functions on μ-oxo bridging oxides, and the 6-31G basis set is applied for the rest of the atoms in the QM layer. Such a combination of basis sets has been validated through extensive benchmark calculations on high-valent manganese complexes.[9,27,45]

Geometry Optimization. Fully relaxed QM/MM molecular structures are obtained at the ONIOM-EE (UHF B3LYP/lacvp,6-31G(2df),6-31G:AMBER) level of theory by geometry optimization of the complete structural models with standard methods, including Newton–Raphson updating of the second derivative (Hessian) matrix with the Broyden–Fletcher–Goldfarb–Shannon strategy. A buffer shell of amino acid residues with α-carbons within 15–20 Å from any atom in the OEC ion cluster is harmonically constrained in order to preserve the natural shape of the system.

Electronic States. The electronic states of fully relaxed structural models, obtained at the ONIOM QM/MM level of theory, typically involve antiferromagnetic couplings between manganese centers. These couplings define BS states, providing multiconfigurational character to the electronic states.[46–49] A typical optimization procedure involves both the preparation of the initial spin-electronic state and the subsequent geometry relaxation, carried out at the ONIOM DFT-QM/MM level of theory. The optimization process preserves the purity of the initial state when there are no other spin states of similar energy found along the optimization process, since the state is compatible with the geometry of the Mn cluster and the specific arrangement of ligands.

2.3. EXAFS Simulations. Simulations of EXAFS spectra allow one to partially validate the proposed DFT QM/MM structural models of S-state intermediates in terms of direct comparisons with high-resolution experimental data.[16,17,19] The simulations involve solving the multi-scattering problem associated with the photoelectrons emitted by the Mn ions, upon X-ray absorption.[9] The quantum mechanical interference of outgoing photoelectrons with the scattered waves from atoms surrounding the Mn ions gives rise to local maxima and minima in the oscillations of EXAFS intensities. The Fourier transform of these oscillations determines the Mn–Mn distances, the coordination bond lengths of Mn ions, and the underlying changes in the Mn coordination as determined by changes in the oxidation state of the OEC. It is important to note, however, that due to the limitations of DFT QM/MM structural refinement (with an estimated error in metal–

metal and metal–ligand distances of 0.05 Å), one cannot expect a perfect match between calculated and experimental EXAFS spectra. EXAFS is a high-resolution technique with a distance error on the order of 0.02 Å.

Computational Aspects. Simulations of EXAFS spectra are carried out by using the real space Green's function (RSGF) approach,[50] as implemented in the program *FEFF8*, version 8.2,[51] in conjunction with the DFT QM/MM structural models of S-state intermediates. The oscillatory part of the dipole transition matrix element, or EXAFS data $\chi(k)$, is obtained by using the module *FEFF83*, explicitly considering atoms within 10 Å of any metal in the OEC. The energy axis is converted into the momentum (k) space by using $E_0 = 6547$ eV, considering the energy range from 20 eV above E_0 to the iron K-edge at 7100 eV. In addition, a window function $w(k)$ is applied to the (mostly k^3-weighted) EXAFS data, multiplying $\chi(k)$ by $w(k)$, in order to reduce the so-called "side-loop effect" in the subsequent Fourier transform. The window function is typically a fractional cosine-square window extending over 10 eV at both k-range limits. Finally, the windowed spectra are Fourier-transformed. This procedure is in accordance with previously published EXAFS data.[10,16,18,52]

Theoretical Aspects. The computations of EXAFS spectra are based on the theory of the oscillatory structure due to multiple scattering, originally proposed by Kronig[53,54] and worked out in detail by Sayers,[55] Stern,[56] Lee and Pendry,[57,58] and Ashley and Doniach.[59] In a typical EXAFS experiment, a monochromatic X-ray beam passes through a homogeneous sample of uniform thickness x. The transmitted (I) and incident (I_0) fluxes define the absorption coefficient $\mu(E)$ as follows: $I = I_0 \exp(-\mu(E)x)$, where $\mu(E)$ is the absorption of the isolated atom $\mu_0(E)$ multiplied by a correction factor $\mu = \mu_0(1 + \chi)$, with χ the fractional change in absorption coefficient induced by neighboring atoms.

(45) Sproviero, E. M.; Gascón, J. A.; McEvoy, J. P.; Brudvig, G. W.; Batista, V. S. *J. Inorg. Biochem.* **2005**, *100*, 786–800.
(46) Noodleman, L. *J. Chem. Phys.* **1981**, *74*, 5737–5743.
(47) Noodleman, L.; Davidson, E. R. *Chem. Phys.* **1986**, *109*, 131–143.
(48) Noodleman, L.; Case, D. A. *Adv. Inorg. Chem.* **1992**, *38*, 423–470.
(49) Noodleman, L.; Peng, C. Y.; Case, D. A.; Mouesca, J. M. *Coord. Chem. Rev.* **1995**, *144*, 199–244.
(50) Gonis, A. *Green Functions for Ordered and Disordered Systems*; North Holland: Amsterdam, 1992.
(51) Ankudinov, A. L.; Bouldin, C.; Rehr, J. J.; Sims, J.; Hung, H. *Phys. Rev. B: Condens. Matter Mater. Phys.* **2002**, *65*, 104107–104118.
(52) Dau, H.; Liebisch, P.; Haumann, M. *Anal. Bioanal. Chem.* **2003**, *376*, 562–583.
(53) Kronig, R. *Z. Phys.* **1931**, *70*, 317–323.
(54) Kronig, R. *Z. Phys.* **1932**, *75*, 190–210.
(55) Sayers, D. E.; Stern, E. A.; Lytle, F. W. *Phys. Rev. Lett.* **1971**, *27*, 1204–1207.
(56) Stern, E. *Phys. Rev. B: Condens. Matter Mater. Phys.* **1974**, *10*, 3027–3027.
(57) Pendry, J. *Low Energy Electron Diffraction*; Academic Press: New York, 1974.
(58) Lee, P.; Pendry, J. *Phys. Rev. B: Condens. Matter Mater. Phys.* **1975**, *11*, 2795–2811.
(59) Ashley, C.; Doniach, S. *Phys. Rev. B: Condens. Matter Mater. Phys.* **1975**, *11*, 1279–1288.

The standard EXAFS equation for χ is given, within the context of the single-scattering approximation for the K-edge excitation, as follows:[55]

$$\chi(k) = \text{Im} \sum_i \left(\frac{N_i S_0^2 F_i(k)}{kR_i^2} e^{i(2\kappa R_i + \Phi_i(k))} e^{-2\sigma_i^2 k^2} e^{-2R_i/\lambda(k)} \right) \quad (2)$$

where k is the wave vector modulus for the photoelectron; N_i is the number of atoms of type i at distance R_i from the absorber; the Debye–Waller factor $\exp(-2\sigma_i^2 k^2)$ takes account of fluctuations of distances due to structural and/or thermal disorder, under the assumption of small displacements and Gaussian distributions of distances; the exponential term $\exp(-2R_i/\lambda(k))$ takes account of finite elastic mean free paths of photoelectrons $\lambda(k)$ (between 5 and 10 Å for photoelectron energies of 30 to 1000 eV); S_0^2 is an average amplitude reduction factor (its value usually 0.8–0.9, is the percent weight of the main excitation channel with respect to all possible excitation channels); $F_i(k)$ is a scattering amplitude function characteristic of the ith atom; and $\Phi_i(k)$ is a phase function that takes account of the varying potential field along which the photoelectron moves. Equation 2 is valid in the case of nonoriented samples.

3. Results and Discussion

Results are presented in six subsections. First, Section 3.1 reviews the QM/MM structural models of the OEC in the S_1 state (introduced in ref 9) and the comparison between calculated and experimental EXAFS spectra. Section 3.2 describes the structural models of catalytic intermediates in terms of changes in oxidation states of Mn ions, structural rearrangements in the metal cluster, and changes in the protonation states of water ligands, including a quantitative analysis of structural rearrangements and spin populations in the metal cluster as the OEC advances along the catalytic cycle. Section 3.3 presents the comparison between calculated and experimental EXAFS spectra of S-state intermediates. Section 3.4 discusses the potential role of amino acid residues CP43-R357 and D1-Y161 in the underlying proton-coupled electron-transfer (PCET) mechanism and the proton exit channel. Section 3.5 analyzes the water channel pathways and the suggested mechanism for water attachment to the metal cluster. Finally, Section 3.6 compares the proposed mechanism to other proposals recently discussed in the literature.

3.1. QM/MM Structural Models of the S_1 State. Oxidation States. Two DFT-QM/MM models corresponding to redox states of comparable energy were found, including the state Mn-(1) = IV, Mn(2) = IV, Mn(3) = III, Mn(4) = III, or Mn$_4$ (IV,-IV,III,III), where the dangler Mn(4) is pentacoordinated (Figure 3, right) and the state Mn$_4$ (IV,III,III,IV) where an additional water ligand completes the hexacoordinated shell of Mn(4). The relative stability of the two isomers is determined by the strained coordination of H332 to the Mn cluster. The hexacoordinated Mn(2) stabilizes the oxidation state IV only when Mn(4) is pentacoordinated and the oxidation state III (with a Jahn–Teller elongation along the Mn-H332 axis) when the coordination sphere of Mn(4) is complete. These results are consistent with EPR and X-ray spectroscopic evidence, [60–66] but disagree with
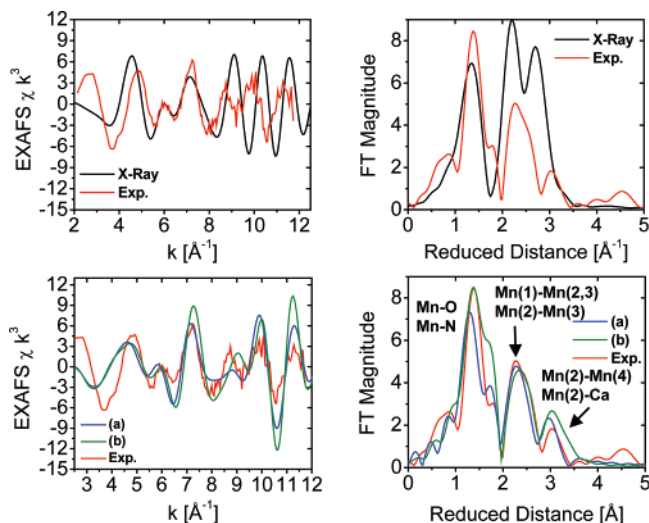

Figure 4. Comparison between the experimental (red) EXAFS spectrum of the OEC of PSII in the S_1 state[16–18] and the simulated spectra of the X-ray diffraction structure (black, upper panel) and the DFT QM/MM models (blue and green, lower panels).

alternative low-valent Mn$_4$ (III,III,III,III) state proposals.[67,68] The two DFT-QM/MM models are neutral in the S_1 state and predict antiferromagnetic coupling between Mn(1) and Mn(2), between Mn(2) and Mn(3), and between Mn(3) and Mn(4), but frustrated spin-coupling between Mn(1) and Mn(3) in the cuboidal structure.

EXAFS Spectra. Figure 4 shows the comparison between experimental (red) and simulated EXAFS spectra of the OEC of PSII in the S_1 state, as described by the 1S5L X-ray diffraction model of Ferreira et al.[15] (black) and the two DFT-QM/MM structural models (blue (a) and green (b)), including EXAFS spectra in momentum (k) space (left) as well as the corresponding spectra in reduced distance (R) space (right) as obtained by Fourier transform of the k-space spectra (experimental data kindly provided by Prof. Holger Dau).[16–18] The simulated EXAFS spectrum obtained with the X-ray model structure (Figure 4, top) shows less agreement with the experimental EXAFS spectrum than the spectra obtained with the QM/MM models, mainly due to the incomplete coordination of the metal centers in the X-ray model. Also, the second and third peaks are shifted and with higher amplitude due to the slightly different geometry of the metal cluster. In contrast, the EXAFS spectra based on both QM/MM models show qualitative agreement with experimental data, including the description of the peaks associated with multiscattering from the N and O Mn–ligand centers at ~1.8 Å (reduced distances ~1.4 Å), the short Mn–Mn distances at ~2.7 Å (reduced distances ~2.3 Å) characteristic of PSII, and backscattering due to the dangling Mn and Ca^{2+} at >3 Å. The main difference between the two

(60) Dau, H.; Iuzzolino, L.; Dittmer, J. *Biochim. Biophys. Acta* **2001**, *1503*, 24–39.
(61) Ono, T. A.; Noguchi, T.; Inoue, Y.; Kusunoki, M.; Matsushita, T.; Oyanagi, H. *Science* **1992**, *258*, 1335–1337.
(62) Yachandra, V. K.; DeRose, V. J.; Latimer, M. J.; Mukerji, I.; Sauer, K.; Klein, M. P. *Science* **1993**, *260*, 675–679.
(63) Roelofs, T. A.; Liang, W. C.; Latimer, M. J.; Cinco, R. M.; Rompel, A.; Andrews, J. C.; Sauer, K.; Yachandra, V. K.; Klein, M. P. *Proc. Natl. Acad. Sci. U.S.A.* **1996**, *93*, 3335–3340.

(64) Bergmann, U.; Grush, M. M.; Horne, C. R.; DeMarois, P.; Penner-Hahn, J. E.; Yocum, C. F.; Wright, D. W.; Dube, C. E.; Armstrong, W. H.; Christou, G.; Eppley, H. J.; Cramer, S. P. *J. Phys. Chem. B* **1998**, *102*, 8350–8352.
(65) Iuzzolino, L.; Dittmer, J.; Dau, H. *Biochemistry* **1998**, *37*, 17112–17119.
(66) Messinger, J.; Robblee, J. H.; Bergmann, U.; Fernandez, C.; Glatzel, P.; Visser, H.; Cinco, R. M.; McFarlane, K. L.; Bellacchio, E.; Pizarro, S. A.; Cramer, S. P.; Sauer, K.; Klein, M. P.; Yachandra, V. K. *J. Am. Chem. Soc.* **2001**, *123*, 7804–7820.
(67) Zheng, M.; Dismukes, G. C. *Inorg. Chem.* **1996**, *35*, 3307–3319.
(68) Kuzek, D.; Pace, R. J. *Biochim. Biophys. Acta* **2001**, *1503*, 123–137.

simulated EXAFS spectra (see blue and green lines for the FT magnitude as a function of reduced distance) is the slightly different structure of the first prominent peak at reduced distances ~1.6 Å, where model b has a more pronounced shoulder due to the slightly shorter 2.1 Å coordination bond length between Mn(2) and the carboxylate oxygens of E333, while the corresponding bond length in model a is 2.2 Å.

Ligation Scheme. In contrast to the ligation scheme proposed by the XRD structure (Figure 3, left), the QM/MM models involve metal ions with the usual number of ligands (i.e., 5 and 6 ligands coordinated to Mn ions with oxidation states III and IV, respectively, and 7−8 ligands attached to Ca^{2+} which usually ligates to 6−8 ligands (Figure 3, right)). In the QM/MM models, the proteinaceous ligation includes η^2-coordination of E333 to both Mn(3) and Mn(2) and hydrogen bonding to the protonated CP43-E354 (neutral state); monodentate coordination of D342, CP43-E354, and D170 to Mn(1), Mn(3), and Mn(4), respectively; and ligation of E189 and H332 to Mn(2).

Hydration. The QM/MM models were hydrated by "soaking" the molecular structures in a bath of thermally equilibrated water molecules, keeping the water molecules that did not sterically interfere with the protein residues or bound water molecules. The hydrated structures were subsequently relaxed by geometry optimization, and the procedure of soaking and relaxation was iterated until the number of water molecules converged. The hydration protocol resulted in the addition of water molecules attached to Ca and Mn ions in the cuboidal Mn₄Ca cluster as well as several water molecules establishing a hydrogen-bond network approaching the Mn₄Ca cluster from the lumen. The resulting hydration completed the coordination spheres of Ca and Mn ions and was roughly consistent with pulsed EPR experiments revealing the presence of several exchangeable deuterons near the Mn cluster in the S_0, S_1, and S_2 states.[26] However, the QM/MM models predict more water/hydroxo ligands than that suggested by EPR measurements, with about six such exchangeable protons.

Substrate Water Binding. The QM/MM models include potential substrate water molecules not resolved in the XRD structures. These water molecules are ligated to Ca^{2+} and Mn-(4), as suggested by mechanistic ideas (see Figure 3, right)[9,11,21] and the electronic density originally assigned to bicarbonate.[15] The respective oxygen atoms of the two substrate water molecules are approximately 2.6 Å apart and are brought yet closer together in the S_4 state (following deprotonation of the Mn-bound water) to achieve O=O bond formation in the $S_4 \rightarrow S_0$ transition (see Section 3.2).

Bicarbonate Binding. As mentioned before, the QM/MM hybrid models assign the 1S5L electronic density originally assigned to bicarbonate to substrate water molecules bound to Mn(4) and Ca^{2+}. The bicarbonate ion has not been included in the QM/MM hybrid models since the docking site proposed by the 1S5L XRD structure was considered adventitious. In fact, bicarbonate was not seen in the more recently published XRD structure.[30]

Chloride Binding. In contrast to the XRD structures where small ligands were not resolved, the QM/MM hybrid models include a calcium-bound chloride ligand docked similarly to acetate.[8,9,11] These QM/MM structures predict that Cl^- is not directly bound to a Mn center but rather loosely bound to the metal cluster by electrostatic interactions, at approximately 5

Å from the nearest Mn center. The QM/MM binding site of Cl^- is consistent with the pulsed EPR data of the OEC, where chloride has been replaced by acetate and a distance of about 3.2 Å was measured between the acetate methyl group and tyrosine Z.[69] In addition, the proposed Cl^- binding site is partially consistent with recent experiments indicating that Cl^- is not a first-sphere Mn ligand.[70]

Interatomic Distances. A quantitative analysis of interatomic bond lengths and bond orientation angles relative to the membrane normal, including interatomic distances and bond orientations obtained at the ONIOM-EE (UHF B3LYP/lacvp,6-31G(2df),6-31G:AMBER) level of theory and the corresponding structural parameters in the X-ray diffraction structure 1S5L (Figure 3),[15] indicates that the configuration of the cuboidal Mn₃-CaO₄Mn complex proposed by the QM/MM hybrid model shares common structural features with the XRD model.[9,10] In particular, the root-mean-squared displacement of the QM/MM structural model, relative to the X-ray diffraction structure proposed by Ferreira et al.,[15] is only 0.6 Å in length. Therefore, as pointed out earlier,[9] it is difficult to judge whether the oxomanganese complexes in the QM/MM model and in the XRD structure are truly identical or whether there are any significant differences.

Considering the small structural differences between models a and b, we limit the presentation of the remaining results in this paper to structures obtained from model a. Analogous results can be obtained for model b with an additional water ligand attached to the dangling Mn(4) atom.

Comparisons with Polarized EXAFS Studies. Recent studies based on polarized EXAFS experiments have proposed four possible molecular structures of the Mn₃O₄CaMn inorganic core of the OEC (i.e., models I, II, IIa, and III, described in ref 71). The models have been obtained from the analysis of orientation-dependent differences in polarized EXAFS measurements and are currently considered to be the most rigorous empirical models of the inorganic core developed to date. Placing any of these EXAFS models into the XRD structures, however, results in unsatisfactory metal−ligand distances, coordination numbers, and geometries.[71] In addition, model I is less likely to be correct since the Mn−Ca vectors are not along the membrane normal.

Considering that the inorganic core of the DFT-QM/MM model is fully consistent with the proteinaceous ligation proposed by the XRD structures and that multiple molecular models can yield similar EXAFS spectra, it is of interest to compare the isotropic EXAFS spectra of the four models suggested by Yano et al.[71] to the corresponding spectra obtained with the inorganic core of the DFT-QM/MM model.

Figure 5 shows the comparison of calculated EXAFS spectra for the four models of the inorganic core Mn₄O₄Ca, suggested by Yano et al.[71] (i.e., models I, II, IIa, and III) and the corresponding EXAFS spectrum of the DFT-QM/MM inorganic core isolated from the protein environment. These results show that the isotropic EXAFS spectra of the models suggested by Yano et al. exhibit amplitude differences among themselves

(69) Force, D. A.; Randall, D. W.; Britt, R. D. *Biochemistry* **1997**, *36*, 12062−12070.
(70) Haumann, M.; Barra, M.; Loja, P.; Löscher, S.; Krivanek, R.; Grundmeier, A.; Dau, L. E. A. H. *Biochemistry* **2006**, *45*, 13101−13107.
(71) Yano, J.; Kern, J.; Sauer, K.; Latimer, M. J.; Pushkar, Y.; Biesiadka, J.; Loll, B.; Saenger, W.; Messinger, J.; Zouni, A.; Yachandra, V. K. *Science* **2006**, *314*, 821−225.
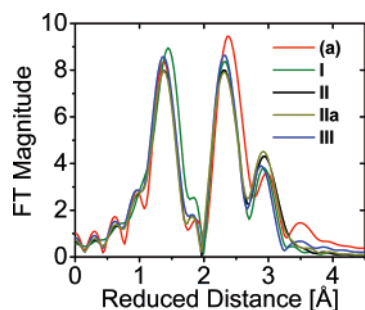
Figure 5. Comparason of calculated EXAFS spectra associated with the oxomanganese complex of PSII described by structures I, II, IIa, and III, proposed by Yano et al.[17] (green, black, dark yellow, and blue, respectively) and model a, obtained according to DFT QM/MM hybrid methods (red).

Table 1. Interionic Distances and Bond Angles Relative to the Membrane Normal in the DFT QM/MM Structural Models of the OEC of PSII in the S_0, S_2, S_3, and S_4 States

bond vector	S_0		S_2		S_3		S_4	
	length (Å)	angle (deg)	length (Å)	angle (deg)	length (Å)	angle (deg)	length (Å)	angle (deg)
Mn(1)−Mn(2)	2.65	59	2.78	58	2.69	57	2.69	54
Mn(1)−Mn(3)	2.92	76	2.77	81	2.81	73	2.82	74
Mn(2)−Mn(3)	2.96	78	2.86	65	2.82	77	2.58	72
Mn(2)−Mn(4)	3.79	54	3.29	59	3.84	58	3.55	61
Mn(3)−Mn(4)	3.04	21	3.55	35	2.81	21	2.81	27
Ca−Mn(2)	3.59	63	3.78	57	3.63	63	3.61	71
Ca−Mn(3)	3.51	50	4.00	36	3.74	53	3.58	57

which are comparable to the observed deviations relative to the spectrum of the DFT-QM/MM model. Therefore, on the basis of the isotropic EXAFS spectra, it is difficult to judge whether there are any significant spectroscopic differences between the QM/MM and polarized-EXAFS models. A more systematic comparative analysis would require comparisons of polarized EXAFS associated with different orientations of the cluster. Such a study will be presented elsewhere.

Comparisons with FTIR Studies. The ligation scheme proposed by the DFT QM/MM models suggests that several amino acid residues, including D1-E189, CP43-E354, D1-E333, D1-D170, D1-D342, and D1-H332 are directly ligated to Mn centers, in partial agreement with XRD models.[15,30] However, it is not yet clear whether the proposed ligation scheme is consistent with FTIR studies. Experiments combining mutagenesis and FTIR measurements have shown no evidence of vibrational frequency shifts for amino acid residues D1-D170, D1-D342, and D1-E189 as the OEC is advanced from the S_0 to the S_3 states.[72−76] The simplest interpretation of these experiments is that none of these amino acid residues are ligated to the Mn ions that undergo oxidation during the S_0−S_3 transitions, in marked disagreement with QM/MM and XRD models. However, such an interpretation remains uncertain since there has been a lack of systematic studies on the influence that oxidation of Mn centers has on the vibrational frequencies of carboxylate ligands coordinated to the metal center in high-valent oxomanganese complexes.

In order to evaluate whether the DFT-QM/MM ligation scheme is consistent with FTIR data, it is necessary to perform a complete vibrational analysis of the ligated OEC along the catalytic cycle. While such a study is still ongoing in our group, preliminary results on benchmark model systems already indicate that the vibrational frequencies of carboxylate ligands are often insensitive to changes in the oxidation states of Mn centers. The most significant vibrational frequency shifts, induced by oxidation of a Mn(III) center, correspond to the asymmetric mode of a carboxylate ligand coordinated along the Jahn−Teller axis of Mn(III). However, such a coordination

mode is unusual since carboxylate groups are strong ligands that tend to leave weaker-binding ligands, such as water, to bind along the Jahn−Teller axes. In fact, as described in Section 3.2, neither D1-D170, D1-D342, or D1-E189 are predicted to be ligated along the Jahn−Teller axis of a Mn center when the OEC is in the S_0−S_3 states. Therefore, these results are consistent with negligible changes in the vibrational frequencies of these carboxylate ligands even when they are directly ligated to the Mn centers oxidized as suggested by the DFT-QM/MM models. The only amino acid residue that is found to be ligated along the Jahn−Teller axis of a Mn^{III} ion is CP43-E354. Therefore, we anticipate that there should be an observable vibrational frequency shift for the asymmetric stretch mode of the carboxylate group of this residue, upon the $S_1 \rightarrow S_2$ transition of the OEC. This prediction, however, remains to be addressed by FTIR measurements.

The vibrational analysis of QM/MM models indicates that most of the observed FTIR vibrational frequency shifts must correspond to amino acid residues that are not directly ligated to the OEC metal cluster. Furthermore, the direct effect of Mn oxidation on the vibrational frequencies of its ligands can be quite moderate. This is contrary to what would be expected from an analysis solely based on formal oxidation numbers, since polarization of the ligand and changes in the partial atomic charges due to charge transfer interactions should at least produce an observable electrostatic influence on the vibrational frequencies of the ligands. However, any kind of correlation between the oxidation states of metal center and their partial ionic charges is highly improbable in oxomanganese complexes, due to the extensive charge delocalization among metal centers.[9,45,77−81] In the particular case of the OEC, we find that the partial ionic charges of manganese centers are not significantly affected or correlated with changes in oxidation states as the system evolves from the S_0 to the S_3 state along the catalytic cycle (see Table 2). Changes in the overall charge of the metal cluster, however, can induce vibrational frequency shifts associated with ligands involved in charge-transfer interactions (e.g., D1-Ala344 upon $S_1 \rightarrow S_2$ oxidation). Vibrational frequency shifts can also be indirectly induced by the resulting molecular rearrangements, changes in protonation

(72) Debus, R. J.; Strickler, M. A.; Walker, L. M.; Hillier, W. *Biochemistry* **2005**, *44*, 1367−1374.
(73) Chu, H.; Debus, R. J.; Babcock, G. T. *Biochemistry* **2001**, *40*, 2312−2316.
(74) Strickler, M. A.; Hillier, W.; Debus, R. J. *Biochemistry* **2006**, *45*, 8801−8811.
(75) Strickler, M. A.; Walker, L. M.; Hillier, W.; Britt, D.; Debus, R. *J. Biochemistry* **2007**, *46*, 3151−3160.
(76) Kimura, Y.; Mizusawa, N.; Yamanari, T.; Ishii, A.; Ono, T. *J. Biol. Chem.* **2005**, *280*, 2078−2083.

(77) McGrady, J. E.; Stranger, R. *J. Am. Chem. Soc.* **1997**, *119*, 8512−8522.
(78) Zhao, X. G.; Richardson, W. H.; Chen, J. L.; Li, J.; Noodleman, L.; Tsai, H. L.; Hendrickson, D. N. *Inorg. Chem.* **1997**, *36*, 1198−1217.
(79) Delfs, C. D.; Stranger, R. *Inorg. Chem.* **2001**, *40*, 3061−3076.
(80) Barone, V.; Bencini, A.; Gatteschi, D.; Totti, F. *Chem.—Eur. J.* **2002**, *8*, 5019−5027.
(81) Glatzel, P.; Bergmann, U.; Yano, J.; Visser, H.; Robblee, J. H.; Gu, W.; Groot, F. D.; Christou, G.; Pecoraro, V. L.; Cramer, S. P.; Yachandra, V. K. *J. Am. Chem. Soc.* **2004**, *126*, 9946−9959.

Table 2. Mulliken Spin Population Analysis and ESP Atomic Charges in the DFT QM/MM Models of the OEC of PSII in the S_0, S_2, S_3, and S_4 States

ion center	S_0			S_2			S_3			S_4		
	spin pop	oxid no.	ESP charge	spin pop	oxid no.	ESP charge	spin pop	oxid no.	ESP charge	spin pop	oxid no.	ESP charge
Mn(1)	−2.88	+4	+1.30	−2.79	+4	+1.14	+2.87	+4	+1.38	+2.85	+4	+1.32
Mn(2)	+3.83	+3	+1.20	+2.92	+4	+1.02	−3.15	+4	+1.16	−3.19	+4	+1.72
Mn(3)	−3.87	+3	+1.27	−2.74	+4	+1.59	+2.97	+4	+1.62	+2.84	+4	+1.72
Mn(4)	+3.80	+3	+1.15	+3.79	+3	+1.49	−2.98	+4	+1.13	−3.10	+4	+0.97
O(5)	−0.00	−2	−0.75	+0.09	−2	−0.53	+0.03	−2	−0.68	+0.03	−2	−0.76
O(6)	−0.05	−2	−0.92	+0.02	−2	−0.81	+0.03	−2	−0.84	+0.01	−2	−0.99
O(7)	+0.00	−2	−0.74	−0.03	−2	−0.78	−0.10	−2	−0.72	−0.07	−2	−0.72
O(8)	0.03	−2	−0.95	−0.09	−2	−0.86	+0.04	−2	−1.11	+0.05	−2	−1.49
Ca	−0.00	+2	+1.60	−0.00	+2	+1.56	−0.00	+2	+1.65	+0.00	+2	+1.66
Cl	0.04	−1	−0.54	+0.00	−1	−0.67	−0.00	−1	−0.68	+0.27	−1	−0.48
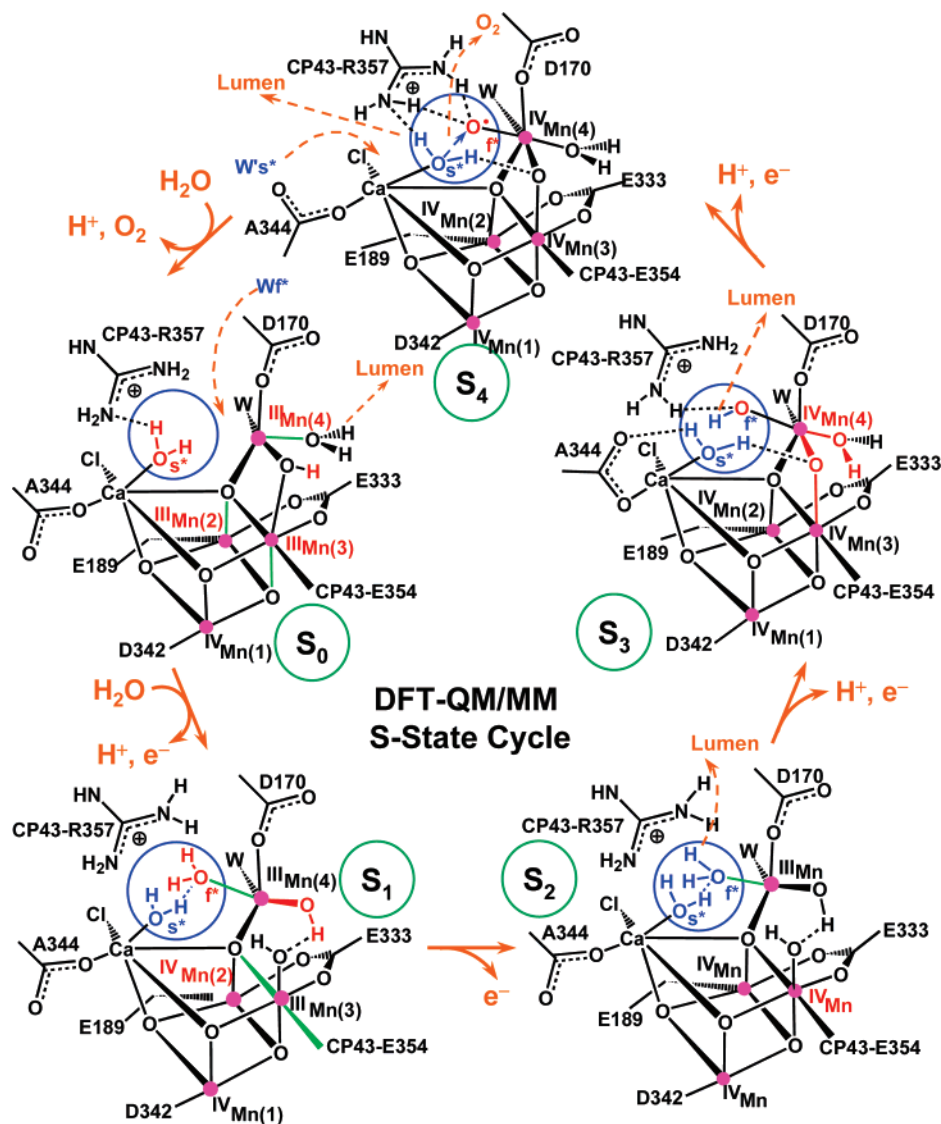
Figure 6. Catalytic cycle of water splitting suggested by DFT QM/MM models of the OEC of PSII. Dashed arrows indicate transformations leading to the following S state in the cycle. Changes caused by an S-state transition are highlighted in red. The blue circles highlight substrate water molecules. Coordination bonds elongated by the Jahn−Teller distortion are marked in green.

states, or hydrogen-bonding patterns induced by oxidation of the metal cluster on surrounding amino acid residues.[82]

3.2. Catalytic Cycle. Figure 6 shows a schematic representation of the catalytic cycle of water splitting as described by

structural rearrangements and changes in oxidation and protonation states in the Mn₃CaO₄ cluster. Dashed arrows indicate transformations leading to the following S state in the cycle. Changes caused by an S-state transition are highlighted in red. The blue circles highlight substrate water molecules, and coordination bonds elongated by the Jahn−Teller distortion are

(82) Law, N. A.; Hillier, W.; Chu, H.; Hsieh, W.; Haymond, S.; Cerda, J.; Pecoraro, V.; Babcock, G. *J. Inorg. Biochem.* **2001**, *86*, 310−320.
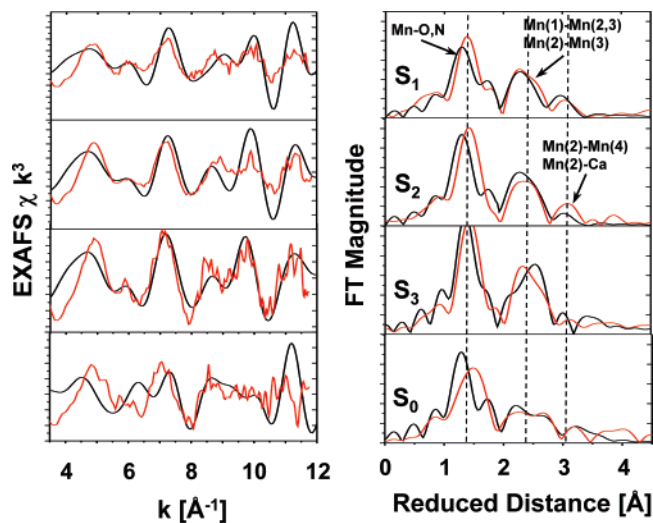
Figure 7. Comparison between experimental[16-18] (red) and calculated (black) EXAFS spectra corresponding to the catalytic cycle of water splitting at the OEC of PSII. Left panel: *k*-weighted EXAFS spectra. Right panel: Fourier-transformed spectra obtained as described in Section 2.3. Spectra in *r* space shows three prominent peaks corresponding to scattering centers in the first (O, N), second (Mn in the core), and third (dangling Mn, Ca) coordination shells of Mn, respectively. Vertical dashed lines are included to facilitate the comparison.

marked in green. A quantitative analysis of the structures and spin-electronic states is presented in Tables 1 and 2. In particular, the spin population analysis, presented in Table 2, shows that the catalytic cycle involves changes in the oxidation states of Mn(2), Mn(3), and Mn(4), while Mn(1) remains redox-inactive throughout the entire cycle. The analysis of ESP charges, presented in Table 2, shows that there is extensive charge transfer between Mn centers and oxo bridges, reducing the partial ionic charges of metal centers and complicating the correlation with oxidation states. The resulting models are validated in terms of simulations of EXAFS spectra and direct comparisons with experimental data, as shown in Figure 7.

$S_0 \rightarrow S_1$ **Transition.** Starting from the most reduced state of the OEC, the $S_0 \rightarrow S_1$ transition involves oxidation of Mn(2), deprotonation of a water molecule ligated to Mn(4), and the attachment of a substrate water molecule to Mn(4). The proposed deprotonation is consistent with electrochromic measurements suggesting that no charge is accumulated in the $S_0 \rightarrow S_1$ transition.[83-85] These rearragements open the protonated μ-oxo bridge between Mn(4) and Mn(3), stretching the Mn-(4)—O distance and leaving the OH^- group ligated to Mn(3). The strengthening of the coordination between Mn(3) and its axial ligand changes the Jahn—Teller elongated bond from axial to equatorial (see highlighted bonds in Figure 6), shortening the Mn(1)—Mn(3) distance and making it similar to the distance Mn(1)—Mn(2). These results are consistent with the EXAFS observation of a single short (2.7 Å) Mn—Mn distance per Mn₄ complex in the S_0 state and two short (2.72 Å) Mn—Mn distances per Mn₄ complex in the S_1 state and another one of about 2.8 Å.[60,62,86,87] The resulting structural changes make the

configurations of the metal cluster in the S_0 and S_1 states significantly different, as observed by EXAFS measurements.[17,88] These results suggest that changes in metal—metal distances, observed by EXAFS spectroscopy, are due to oxidation state transitions inducing changes in the protonation states of the Mn ligands. As discussed in Section 3.1, the additional μ-oxo bridge between Mn(3) and Mn(4) is not present in the XRD models of the S_1 state. Its justification is based on the energy analysis and on the favorable comparison with EXAFS data, not from the crystallographic models. The additional μ-oxo bridge is proposed not only for the QM/MM model of the S_0 state but also for the S_3 and S_4 states and is essential for deprotonation of substrate water molecules.

$S_1 \rightarrow S_2$ **Transition.** Following the catalytic cycle, outlined in Figure 6, the $S_1 \rightarrow S_2$ transition involves oxidation of Mn-(3). This oxidation does not induce significant structural rearrangements, changes in Mn—Mn distances, or deprotonation of the cluster.[83-85,89-92] Therefore, in contrast to all other transions, the cluster accumulates a net positive charge upon $S_1 \rightarrow S_2$ oxidation.

$S_2 \rightarrow S_3$ **Transition.** The $S_2 \rightarrow S_3$ transition releases one proton from a water ligand (e.g., the substrate water molecule bound to Mn(4)), consistent with electrochromism data,[3,32,93-95] and advances the oxidation state of Mn(4) from III to IV, strengthening the interactions between Mn(4) and the OH^- ligand of Mn(3). As a result of these stronger interactions, the μ-oxo bridge between Mn(3) and Mn(4) is formed by proton transfer from the OH^- ligand of Mn(3) to the hydrogen-bonded OH^- ligand of Mn(4). Note that the OH^- proton acceptor, ligated to Mn(4), is regenerated by deprotonation of the water ligand in the $S_0 \rightarrow S_1$ transition, upon opening of the μ-oxo bridge between Mn(3) and Mn(4). The suggested rearrangements, induced by oxidation of Mn(4) and proton transfer, are consistent with the observation that the rate constant is pH-dependent,[96] suggesting that the $S_2 \rightarrow S_3$ transition is "kinetically steered" by proton movements. The rearrangements are also consistent with the observation that the structure of the cluster significantly changes upon formation of the S_3 state, as suggested by EXAFS measurements.[17,97]

$S_3 \rightarrow S_4$ **Transition.** The oxidation state transition $S_3 \rightarrow S_4$ further deprotonates the already partially deprotonated substrate water molecule (bound to the dangling Mn(4) and hydrogen bonded to CP43-R357), releasing another proton to the lumen and changing the charge of the complex as suggested by electrochromic bandshift measurements.[98] The deprotonation of the substrate water molecule first forms the oxyl radical Mn^III—

(83) Kretschmann, H.; Witt, H. T. *Biochim. Biophys. Acta* **1993**, *1144*, 331–345.
(84) Kretschmann, H.; Schlodder, E.; Witt, H. T. *Biochim. Biophys. Acta* **1996**, *1274*, 1–8.
(85) Haumann, M.; Boegershausen, O.; Junge, W. *FEBS Lett.* **1994**, *355*, 101–105.
(86) Pospisil, P.; Haumann, M.; Dittmer, J.; Sole, V. A.; Dau, H. *Biophys. J.* **2003**, *84*, 1370–1386.

(87) Dau, H.; Liebisch, P.; Haumann, M. *Anal. Bioanal. Chem.* **2003**, *376*, 562–583.
(88) Robblee, J. H.; Messinger, J.; Cinco, R. M.; McFarlane, K. L.; Fernandez, C.; Pizarro, S. A.; Sauer, K.; Yachandra, V. K. *J. Am. Chem. Soc.* **2002**, *124*, 7459–7471.
(89) Fowler, C. F. *Biochim. Biophys. Acta* **1977**, *462*, 414–421.
(90) Wille, B.; Lavergne, J. *Photobiochem. Photobiophys.* **1982**, *4*, 131–144.
(91) Saphon, S.; Crofts, A. R. Z. *Naturforsch* **1977**, *32C*, 617–626.
(92) Rappaport, F.; Blanchard-Desce, M.; Lavergne, J. *Biochim. Biophys. Acta* **1994**, *1184*, 178–192.
(93) Junge, W.; Haumann, M.; Ahbrink, R.; Mulkidjanian, A.; Clausen, J. *Philos. Trans. R. Soc. London, Ser. B* **2002**, *357*, 1407–1418.
(94) Schlodder, E.; Witt, H. T. *J. Biol. Chem.* **1999**, *274*, 30877–30392.
(95) Haumann, M.; Junge, W. *Oxygenic Photosynthesis: The Light Reactions*; Kluwer Academic Publishers: Dordrecht, The Netherlands, 1996.
(96) Haumann, M.; Bögershausen, O.; Cherepanov, D.; Ahlbrink, R.; Junge, W. *Photosynth. Res.* **1997**, *51*, 193–208.
(97) Liang, W. C.; Roelofs, T. A.; Cinco, R. M.; Rompel, A.; Latimer, M. J.; Yu, W. O.; Sauer, K.; Klein, M. P.; Yachandra, V. K. *J. Am. Chem. Soc.* **2000**, *122*, 3399–3412.
(98) Haumann, M.; Junge, W. *Biochemistry* **1994**, *33*, 864–872.

$O^•$ transient species that is subsequently oxidized by $Y_Z^•$ to form the $Mn^{IV}-O^•$ species. Therefore, the QM/MM model indicates that the S_4 state accumulates the fourth oxidizing equivalent in the oxidized substrate water, as a high-spin oxyl radical species $Mn^{IV}-O^•$, not in the dangling Mn(4) as the low-spin state $Mn^V\equiv O$ species. As a matter of fact, we have performed a bond-order analysis based on natural atomic orbitals indicating that the $Mn^{IV}-O^•$ bond is a single covalent dative bond (Wiberg bond index = 1.04).

The question of whether the fourth oxidation equivalent resides on a ligand (or on a Mn center) is still strongly debated, and further work is needed to fully resolve this mechanistic aspect. However, in the proposed QM/MM model of the S_4 state, the fourth oxidizing equivalent is localizd on the deprotonated substrate water ligand of the hexacoordinated dangling Mn atom. This is consistent with the observation that formation of the S_4 state does not involve manganese oxidation or reduction.[99] In addition, the proposed formation of a transient deprotonated species (prior to oxidation by the $Y_Z^•$ species) is consistent with the observation of a kinetically resolvable intermediate in the $S_3 \rightarrow S_0$ transition, within 200 μs after the oxidation of Y_Z and prior to dioxygen formation.[99] The proposed high-spin oxyl radical species is also consistent with studies of a biomimetic oxomanganese dimer where the normally pentacoordinated L_4-$Mn^V\equiv O$ becomes hexacoordinated by the coordination of an additional ligand to form the $L_5Mn^{IV}-O^•$ species.[100] Therefore, it is natural to consider that the trans effect, due to coordination of a water ligand trans to the deprotonated water molecule, is an important factor in the stabilization of the oxyl radical state.

$S_4 \rightarrow S_0$ Transition. Finally, the $S_4 \rightarrow S_0$ transition forms dioxygen, by nucleophilic attack of the calcium-bound water molecule on the electrophilic oxyl radical $Mn^{IV}-O^•$. The reaction is promoted by substitution of the calcium-bound water molecule by a water molecule in the second coordination sphere of calcium. This process involves deprotonation of the displaced water, releasing a proton to the lumen via CP43-R357 and transferring the other proton to the basic μ-oxo bridge linking Mn(4) and Mn(3).

The proposed reaction between an activated water molecule bound to Ca^{2+} is similar to earlier proposals by Pecoraro et al.[24] and Brudvig and co-workers.[21] The main difference relative to these other nucleophilic attack models is that in the QM/MM model the nucleophilic water attacks an oxyl radical, rather than an oxo–Mn^V species. Another distinct aspect is that the reaction is promoted by water exchange in the coordination sphere of Ca^{2+} and that the nucleophilic water is activated not only by Ca^{2+} but also by two other basic species, including CP43-R357 and the basic μ-oxo bridge linking Mn(4) and Mn(3).

3.3. EXAFS Spectra of Catalytic Intermediates. Figure 7 shows the comparison of experimental[16–18] and calculated EXAFS spectra of the OEC catalytic intermediates S_0–S_3. The calculated spectra are based on the DFT QM/MM structural models described in Figure 6. Figure 7 (right panel, from top to bottom) shows the evolution of the FT-EXAFS scattering amplitudes for the S states, along the catalytic cycle, as determined by structural rearrangements in the metal cluster,

including changes in the Mn–Mn and Mn–Ca distances and the Mn–ligand coordination bond lengths. The first prominent peak, at reduced distance $\sim$1.4 Å (actual distance $\sim$1.8 Å), is determined by N and O centers directly ligated to Mn ions. This first peak has a shoulder at reduced distance $\sim$1.6 Å (actual distance $\sim$2.1 Å) corresponding to scattering contributions from μ-oxo bridges and the ligated carboxylate group of E333 coordinated to Mn. The second prominent peak, at reduced distance $\sim$2.3 Å (actual distance $\sim$2.7 Å), corresponds to the characteristic Mn–Mn distances in PSII. The width of the second prominent peak at reduced distance $\sim$2.3 Å (actual distance $\sim$2.7 Å) indicates the distribution of short Mn–Mn distances in the manganese cuboidal core. Finally, the third peak at reduced distance $\sim$3.0 Å and beyond corresponds to back-scattering from the dangling Mn and Ca^{2+} at $>$3.3 Å.

The calculated spectra show good qualitative agreement with the experimental spectra obtained by Dau and co-workers[17,101] suggesting that the experimental data can be qualitatively described by the metal–metal distances found in the cuboidal oxomanganese complex. The origin of the observed deviations between simulated and experimental spectra can be traced to the intrinsic limitations of the DFT QM/MM geometry optimization algorithm and the possible contributions from multiple redox isomers of comparable energy.[9] As reported before,[45] DFT(B3LYP) QM/MM-optimized geometries have typical errors of $>$0.05 Å in the description of metal–metal and metal–ligand distances and a few degrees in the description of bond angles, comparable to room-temperature thermal nuclear fluctuations.

The spectra of the S_1 and S_2 states are consistent with two Mn–Mn distances (Mn(1)–Mn(2) and Mn(1)–Mn(3)) shorter than 2.8 Å and a third short Mn–Mn vector (Mn(2)–Mn(3)) slightly longer than 2.8 Å. In the S_0 state, the Mn(1)–Mn(3) vector is longer and the Mn(1)–Mn(2) is shorter than in the S_1 state, splitting the second prominent peak of the FT-EXAFS spectrum according to a bimodal distribution. In the S_3 state, the three Mn–Mn distances become more similar to each other, narrowing the corresponding scattering peak at reduced distance $\sim$2.3 Å.

3.4. Proton-Coupled Electron Transfer (PCET) during S-State Advancement. The advancement of the OEC of PSII throughout the S-state cycle, described in Section 3.2, involves changes in oxidation states of the Mn ions coupled to proton-transfer events that balance the overall charge of the cluster by rearranging the protonation states of the ligands. The direct hydrogen-bonding interactions in the DFT-QM/MM hybrid models, between CP43-R357 and the water ligands responsible for deprotonation, suggest that CP43-R357 is most likely responsible for proton abstraction by functioning as a one-proton gate along the proton-exit channel to the lumen.[22]

Figure 8 schematically shows that CP43-R357 is in close contact with the active face of the OEC, forming part of a hydrogen-bond network that includes both substrate water molecules, the side-chain of CP43-R357, and the calcium-bound chloride ion. Nearby, two hydrogen-bonded nonligating water molecules are found to fit easily into the structure between Mn(4) and D1-D61, which is the first residue of the putative proton-transfer channel leading to the lumenal surface of PSII.

(99) Haumann, M.; Liebisch, P.; Muller, C.; Barra, M.; Grabolle, M.; Dau, H. *Science* **2005**, *310*, 1019–1021.
(100) Lundberg, M.; Blomberg, M. R. A.; Siegbahn, P. E. M. *Inorg. Chem.* **2004**, *43*, 264–274.
(101) Sauer, K.; Yachandra, V. K. *Biochim. Biophys. Acta* **2004**, *1655*, 140–148.
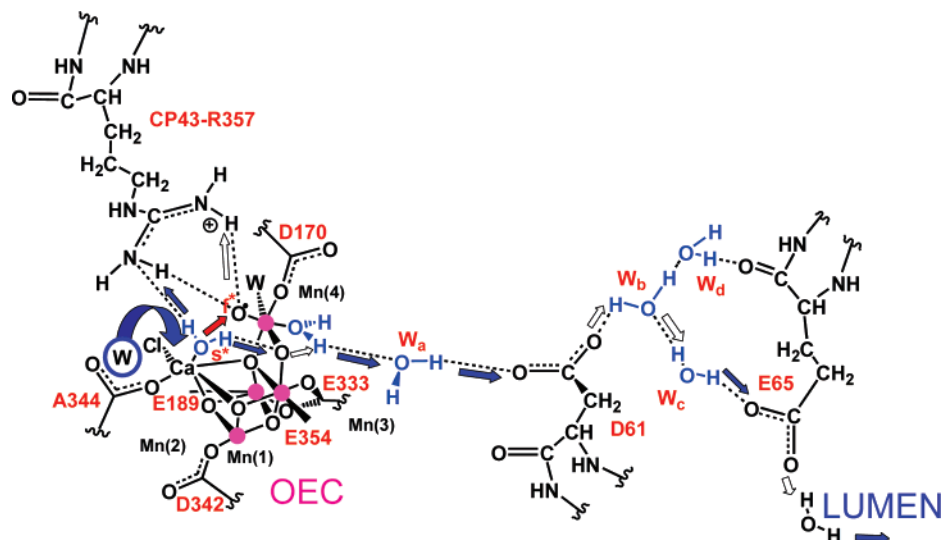
Figure 8. Proton exit channel suggested by the hydrated DFT QM/MM structural models, including a network of hydrogen bonds extended from substrate water molecules "s" (slow) and "f" (fast), via CP43-R357, to the first residue (D1-D61) leading to the lumenal side of the membrane. Proton translocation events are indicated by blue and white arrows and the O=O bond formation event is indicated by a red arrow, promoted by water exchange from Ca^{2+}. Amino acid residues labeled with one-letter symbols correspond to the D1 protein subunit.

The CP43-R357 side chain is thus expected to facilitate the flow of protons from the OEC to the lumenal side of the membrane. This is consistent with its indispensability for O_2 evolution, as demonstrated by mutagenesis studies of PSII from *Synechocystis* sp. PCC 6803 where mutation of the homologous CP43 arginine (CP43-R342) to serine suppressed O_2 evolution.[102] In addition, the arginine side chain is a well-known component of hydrogen-bonding networks in proteins.[103,104] Figure 8 shows that the guanidinium side chain of CP43 R357 is straddling the active face of the metal—oxo cluster, hydrogen bonding with the two putative substrate waters ligated to Ca^{2+} and Mn(4) and also with the putative nonsubstrate ligands (water or hydroxide) of Mn(3) and Mn(4). The ability to hydrogen bond with both substrate and nonsubstrate ligands of Mn(3) and Mn-(4) makes CP43-R357 particularly suitable to facilitate proton translocation from the OEC to the beginning of the proton exit pathway.

An important aspect of the proposed reaction mechanism is the role played by the OH^- ligand of Mn(3) during the deprotonation of substrate water molecules (see Figure 6). During the $S_2 \rightarrow S_3$ transition, the OH^- ligated to Mn(3) deprotonates by proton transfer to an OH^- ligand of Mn(4), transforming such a ligand into a water and forming a μ-oxo bridge between Mn(3) and Mn(4). This induces a rearrangement of hydrogen bonds. The hydrogen bond between the two substrate water molecules is broken and two hydrogen bonds are formed, including a bond between W^{slow} and the μ-oxo bridge and another one between W^{fast} and CP43-R357. Upon deprotonation of W^{fast} via CP43-R357, in the $S_3 \rightarrow S_4$ transition, W^{slow} forms a hydrogen bond with CP43-R357 in addition to its hydrogen bond with the μ-oxo bridge, establishing two deprotonation pathways. During the $S_4 \rightarrow S_0$ transition, one proton transfers to the lumen via CP43-R357 while the other

one translocates to the μ-oxo bridge and subsequently forms the OH^- ligand of Mn(3) upon opening of the bridge in the $S_0 \rightarrow S_1$ transition.

The QM/MM structural models of PSII are also consistent with the hypothesis that D1–Y161 (Y_Z) is an electron transport cofactor, judging by the proximity of Y_Z to the Mn cluster. Simple inspection of the QM/MM structural models (see Figure 3, right) also indicates that the phenoxy oxygen of Y_Z is close to the chloride ligand (3.4 Å apart) and Cl^- is positioned 3.14 Å from Ca^{2+}. Furthermore, the Y_Z phenol group is hydrogen-bonded to the imidazole ϵ-N of the H190 side chain. This hydrogen-bonding partnership is consistent with mutational and spectroscopic studies[105–107] as well as with earlier studies based on MM models.[8,11] These results are consistent with the fact that D1–Y161 has long been viewed as an electron transport cofactor. The oxidized state $P680^+$ is thought to be reduced by the redox-active tyrosine D1-Y161 which in turn is reduced by an electron from the "3 + 1 Mn tetramer".[13,14]

Considering the potential functional roles of CP43-R357 and D1-Y161, it is natural to expect that as the catalytic cycle progresses, PCET might take place by passing electrons from the cluster to the oxidized $Y_Z^{\bullet}$ and protons to CP43-R357. These two charge-transfer processes might be coupled by the modulation of the pKa's of water ligands and nearby amino acid residues (e.g., CP43-R357), induced by changes in the oxidation state of the cluster, as observed in our preliminary calculations of pKa's based on multi-conformation continuum electrostatics methods. The underlying PCET mechanism is also consistent with a recent study of the energetic of the proton exit pathway,[108] but disagrees with earlier proposals where Y_Z was thought to abstract hydrogen atoms from the OEC cluster in every one of

(102) Knoepfle, N.; Bricker, T. M.; Putnam-Evans, C. *Biochemistry* **1999**, *38*, 1582−1588.
(103) Puustinen, A.; Wikstrom, M. *Proc. Natl. Acad. Sci. U.S.A.* **1999**, *96*, 35−37.
(104) Qian, J.; Mills, D. A.; Geren, L.; Wang, K.; Hoganson, C. W.; Schmidt, B.; Hiser, C.; Babcock, G. T.; Durham, B.; Millett, F.; Ferguson-Miller, S. *Biochemistry* **2004**, *43*, 5748−5756.

(105) Roffey, R. A.; Kramer, D. M.; Govindjee,; Sayre, R. T. *Biochim. Biophys. Acta* **1994**, *1185*, 257−270.
(106) Hays, A. M. A.; Vassiliev, I. R.; Golbeck, J. H.; Debus, R. J. *Biochemistry* **1998**, *37*, 11352−11365.
(107) Hays, A. M. A.; Vassiliev, I. R.; Golbeck, J. H.; Debus, R. J. *Biochemistry* **1998**, *38*, 11851−11865.
(108) Ishikita, H.; Saenger, W.; Loll, B.; Biesiadka, J.; Knapp, E. W. *Biochemistry* **2006**, *45*, 2063−2071.
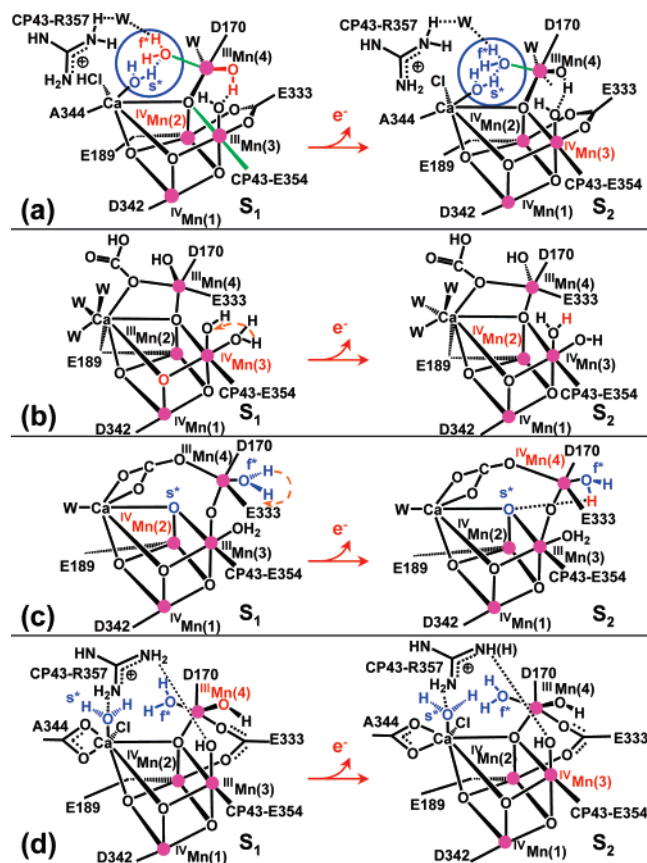
Figure 9. Water channel pathways for substrate water molecules that ligate to Ca^{2+} and the dangling Mn(4) of the OEC in PSII, during the $S_4 \rightarrow S_0$ and $S_0 \rightarrow S_1$ transitions, respectively.

the S-state transitions.[109] The possibility that Y_Z would simultaneously oxidize and deprotonate the hydrated OEC[110] would require a mechanism in which Y_Z abstracts hydrogen atoms and delivers protons to the protein surface via H190. However, based on the lack of a H-bonded pathway leading from H190 to the lumen, it is more likely that H190 accepts a proton from Y_Z during its oxidation and returns the proton to Y_Z on its reduction.

The proposed charge-transfer mechanism is also consistent with a considerable amount of experimental evidence suggesting that there is a discontinuity in the mechanism of S-state advancement beyond the S_2 state. First, only transitions beyond S_2 are blocked by the absence of calcium or chloride or by the presence of acetate.[111-113] Second, electron transfer (ET) between the OEC and P680•+ is significantly slower (and biphasic) in the S-state transitions beyond S_2 than in the early S states.[114] Third, the reorganization energies of the two higher S-state transitions are found to be significantly higher than those of the two previous transitions.[115] Finally, the submicrosecond ET rates from the cluster to P680•+ (via Y_Z) vary much more with temperature in post-S_2 transitions than in the pre-S_2 steps.[116]

(109) Hoganson, C. W.; Lydakis-Simantiris, N.; Tang, X. S.; Tommos, C.; Warncke, K.; Babcock, G. T.; Diner, B. A.; McCracken, J.; Styring, S. *Photosynth. Res.* **1995**, *46*, 177−184.
(110) Hoganson, C. W.; Babcock, G. T. *Science* **1997**, *277*, 1953−1956.
(111) Szalai, V. A.; Brudvig, G. W. *Biochemistry* **1996**, *35*, 15080−1507.
(112) Wincencjusz, H.; van Gorkom, H. J.; Yocum, C. F. *Biochemistry* **1997**, *36*, 3663−3670.
(113) Kühne, H.; Szalai, V. A.; Brudvig, G. W. *Biochemistry* **1999**, *38*, 6604−6613.
(114) Brettel, K.; Schlodder, E.; Witt, H. T. *Biochim. Biophys. Acta* **1984**, *766*, 403−415.
(115) Renger, G.; Christen, G.; Karge, M.; Eckert, H. J.; Irrgang, K. D. *J. Biol. Inorg. Chem.* **1998**, *3*, 360−366.
(116) Jeans, C.; Schilstra, M. J.; Klug, D. R. *Biochemistry* **2002**, *41*, 5015−5023.

Figure 10. Comparison between different proposals for the $S_0 \rightarrow S_1$ transition of the OEC of PSII; including the QM/MM model presented in this work (a); and the models previously proposed by Siegbahn (b);[28,118] Messinger (c);[20] and Brudvig (d).[5,22] The orientation of the metal cluster is the same as that in Figure 3, where the labels for Mn(1), M(2), Mn(3), and Mn(4) are clearly indicated.

These observations might be partially rationalized by the development of a positive charge in the OEC upon S_1−S_2 oxidation.[21]

3.5. Water Channel Pathways. As mentioned in Section 1, the OEC turns over very rapidly and produces up to 50 molecules of O_2 per second. The efficient production of O_2 thus requires an input flux of up to 100 water molecules per second from the lumen. To date, however, the water channel pathways and the mechanism for water attachment to the metal cluster remain poorly understood.

As discussed in Section 3.2, the DFT-QM/MM structural models suggest that the two substrate water molecules ligate to the metal cluster at different S-state transitions. Furthermore, the structural analysis of these QM/MM models suggest that the two water molecules approach the metal cluster from the lumen along two distinct pathways of hydrogen-bonded water molecules (see Figure 9). Surprisingly, however, the channels are embedded in a low-dielectric protein environment and neither of the two pathways correspond to the proposed proton exit channel, depicted in Figure 8.[9,10,15,108]

The analysis of the structure of hydrogen bonds in the channels indicates that each water molecule has (on average) only 2−3 hydrogen bonds—i.e., each water molecule is linked to the molecule in front and behind it along the network but is not hydrogen bonded to surrounding amino acid residues. The incomplete hydrogen-bonding structure establishes optimum conditions for water mobility along the channel, minimizing

Figure 11. Comparison between different proposals for the $S_1 \rightarrow S_2$ transition of the OEC of PSII; including the QM/MM model presented in this work (a); and the models previously proposed by Siegbahn (b);[28,118] Messinger (c);[20] and Brudvig (d).[5,22] The orientation of the metal cluster is the same as that in Figure 3, where the labels for Mn(1), M(2), Mn(3), and Mn(4) are clearly indicated.

Figure 12. Comparison between different proposals for the $S_2 \rightarrow S_3$ transition of the OEC of PSII; including the QM/MM model presented in this work (a); and the models previously proposed by Siegbahn (b);[28,118] Messinger (c);[20] and Brudvig (d).[5,22] The orientation of the metal cluster is the same as that in Figure 3, where the labels for Mn(1), M(2), Mn(3), and Mn(4) are clearly indicated.

the number of competitive hydrogen bonding interactions with the surrounding amino acid residues and enhancing the attachment of water to the metal cluster. In fact, the quantitative analysis of water exchange potential energy profiles shows that the incomplete solvation of water molecules (with only 2–3 hydrogen bonds in the low-dielectric protein environment) increases the binding affinity and the overall water exchange energy barriers as compared with water exchange in biomimetic oxo–manganese complexes in solution.[12] These results suggest that the protein environment surrounding the OEC might have been optimized by natural selection to enhance water binding to the catalytic center. The low dielectric protein environment also stabilizes the coordination of Cl⁻ to the ionic cluster as well as the coordination of the oxomanganese cluster to the carboxylate groups of nearby proteinaceous ligands.

Upon dioxygen evolution, the two substrate water molecules attached to the cluster react together, and their neighboring water molecules in the channels are attached to the corresponding metal centers. As mentioned before, one water molecule ligates to Ca^{2+} in the $S_4 \rightarrow S_0$ transition, substituting the activated substrate water molecule and promoting dioxygen formation. The other water molecule ligates to the dangling Mn(4) atom, during the $S_0 \rightarrow S_1$ transition, opening the μ-oxo bridge between Mn(4) and Mn(3). Both of these events produce conformational changes in the cluster, as indicated by EXAFS spectroscopic measurements.[16]
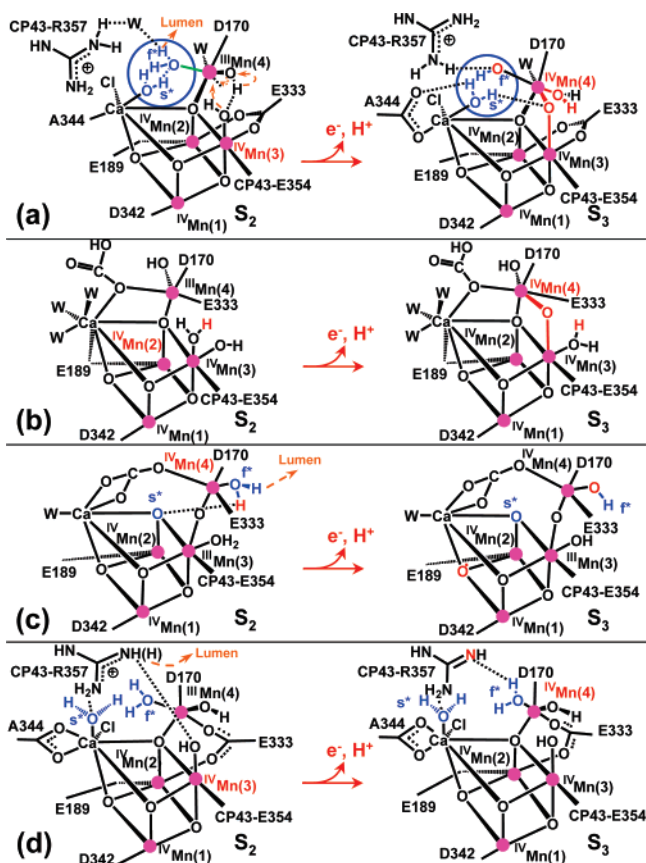
3.6. Comparative Analysis of Catalytic Mechanisms. The catalytic cycle, introduced in Section 3.2, is based only on the analysis of end states along reaction pathways and the favorable comparison between calculated and experimental spectroscopic data for the proposed reaction intermediates. The resulting catalytic cycle includes several aspects common to previously proposed mechanisms (see ref 117 for a review) as well as significant differences. Reviews of more than 40 previously proposed mechanistic models of dioxygen formation, ranging from empirical models to detailed atomic-level scenarios, can be found elsewhere.[5,11,20,22,28,117,118] Here, we limit our discussion to the comparison of the mechanism introduced in Section 3.2 to three other proposals recently discussed in the literature.[5,11,20,22,28,118] The comparison aims to advance the field by providing a working model that fits with experimental data and gives new insights into the chemical steps in the S-state cycle.

In accordance with experiments conducted on various PSII preparations and inorganic model compounds, most oxidizing equivalents are predicted to accumulate in the Mn ions.[21,110] However, one of the oxidizing equivalents is accumulated as a terminal oxyl radical of the dangling manganese atom.[119,120] Formation of the oxyl radical is found to be essential for O–O

(117) Bacon, K. In *Photosynthesis–Photobiochemistry and Photobiophysics*; Kluwer Academic Publishers: Dordretcht, The Netherlands, 2001.
(118) Siegbahn, P. E. M. *Chem.–Eur. J.* **2006**, *12*, 9217–9227.
(119) Siegbahn, P. E. M.; Crabtree, R. H. *J. Am. Chem. Soc.* **1999**, *121*, 117–127.
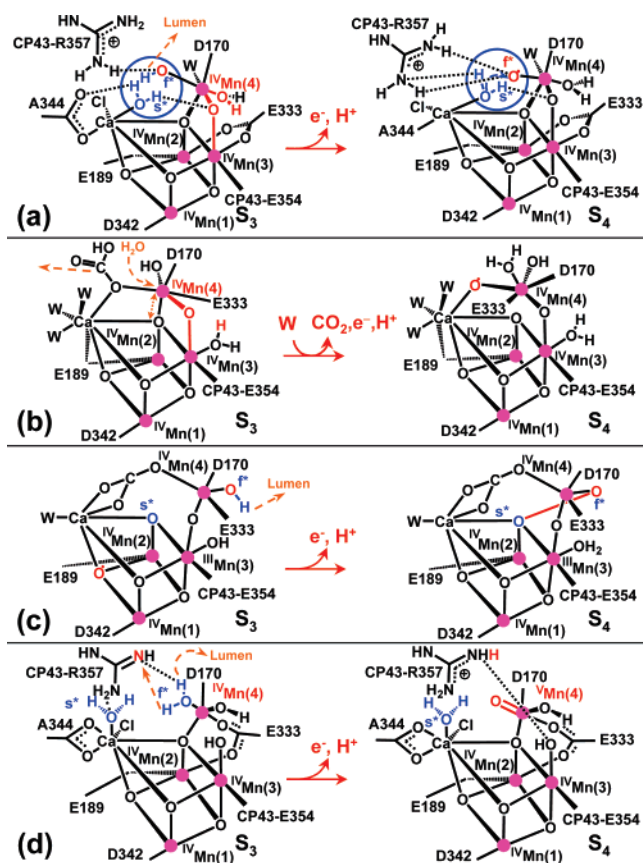(120) Siegbahn, P. E. M. *Curr. Opin. Chem. Biol.* **2002**, *6*, 227–235.

Figure 13. Comparison between different proposals for the $S_3 \rightarrow S_4$ transition of the OEC of PSII; including the QM/MMd model presented in this work (a); and the models previously proposed by Siegbahn (b);[28,118] Messinger (c);[20] and Brudvig (d).[5,22] The orientation of the metal cluster is the same as that in Figure 3, where the labels for Mn(1), M(2), Mn(3), and Mn(4) are clearly indicated.

bond formation but disagrees with other proposals where the oxidation reaction involves species near the cluster[63,121] or a manganese-bridging oxo group.[23] The two substrate water molecules responsible for O=O bond formation are ligated to Ca^{2+} and Mn(4), in agreement with earlier proposals[11,21,22,110] but in disagreement with models where substrate waters are coordinated as oxo bridges between Mn ions.[20,122,123] The overall reaction is also significantly different from other proposals where manganese-bridging oxo ligands react with one another during the O–O bond forming step[122,123] or where basic μ-oxo ligands deprotonate manganese-bound terminal water molecules.[60]

Figures 10–14 show the detailed structural and electronic rearrangements, suggested by the DFT-QM/MM models (panels a), as compared to mechanisms previously proposed by Siegbahn (panels b),[28,118] Messinger (panels c),[20] and Brudvig (panels d).[5,22] Many differences can be noted when comparing the catalytic cycle suggested by the DFT-QM/MM structural models to the other proposals, including differences in the proteinaceous ligation scheme, in the structure of oxo bridges as well as in the description of structural rearrangements and changes in oxidation and protonation states along the cycle. Here, we limit the presentation to a brief comparative overview of the main mechanistic aspects.

(121) Yachandra, V. K. *Philos. Trans. R. Soc. London, Ser. B* **2002**, *357*, 1347–1357.
(122) Brudvig, G. W.; Crabtree, R. H. *Proc. Natl. Acad. Sci. U.S.A.* **1986**, *83*, 4586–4588.
(123) Yachandra, V. K.; Sauer, K.; Klein, M. P. *Chem. Rev.* **1996**, *96*, 2927–2950.
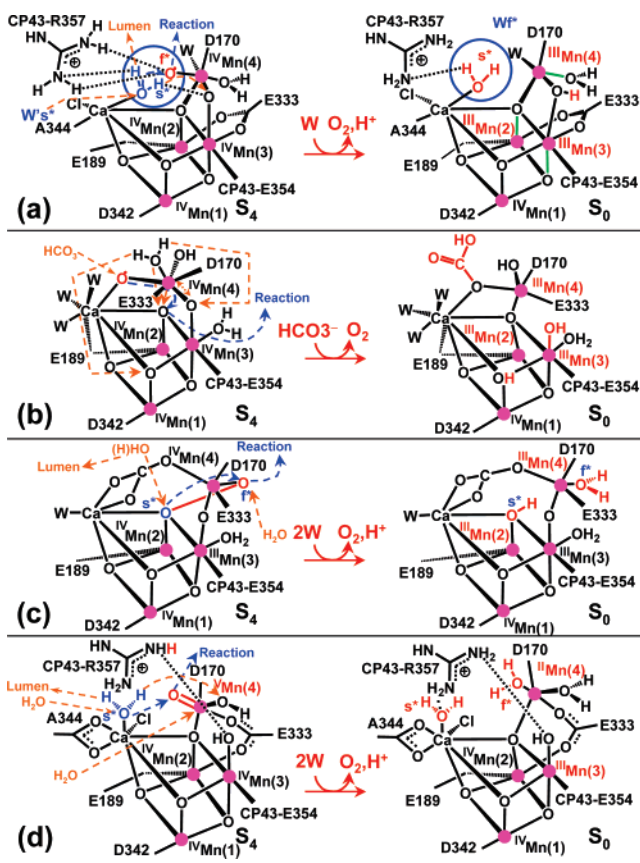
Figure 14. Comparison between different proposals for the $S_4 \rightarrow S_0$ transition of the OEC of PSII; including the QM/MM model presented in this work (a); and the models previously proposed by Siegbahn (b);[28,118] Messinger (c);[20] and Brudvig (d).[5,22] The orientation of the metal cluster is the same as that in Figure 3, where the labels for Mn(1), M(2), Mn(3), and Mn(4) are clearly indicated.

Starting with the S_0 state (see Figure 10), we note that only the QM/MM model suggests that the dangling Mn(4) is coordinated to Mn(3) in the cuboidal cluster by two μ-oxo bridges. One of these bridges is protonated as a result of the deprotonation of a substrate water molecule, during dioxygen formation in the $S_4 \rightarrow S_0$ transition, while the other bridge is also coordinated to Ca^{2+} and Mn(2). In addition, only the QM/MM mechanism predicts that the $S_0 \rightarrow S_1$ transition involves ligation of a substrate water molecule, an event that opens the protonated μ-oxo bridge between Mn(3) and Mn(4) producing conformational changes in the cluster.

A distinct structural/functional feature of the QM/MM model is that the basic μ-oxo bridge, between Mn(3) and Mn(4), deprotonates a calcium-bound terminal water molecule during the $S_4 \rightarrow S_0$ transition. Further translocation of the proton requires opening the protonated μ-oxo bridge, during the $S_0 \rightarrow S_1$ transition, forming a pivotal OH^- ligand of Mn(3) that establishes a hydrogen bond with a basic OH^- ligand of the dangling Mn(4) atom. The latter is involved in a hydrogen-bond network leading to the putative proton-transfer channel to the lumenal surface of PSII, depicted in Figure 8.

Another unique aspect of the QM/MM model is that oxidation of the dangling Mn(4), during the $S_2 \rightarrow S_3$ transition, leads to formation of the μ-oxo bridge between Mn(3) and Mn(4) by proton transfer between the OH^- ligands of Mn(3) and Mn(4). A similar process is proposed by Siegbahn (see Figure 12, panel b), although in that proposal formation of the μ-oxo bridge is

different since it requires double deprotonation of a water ligand of Mn(3), releasing one proton to the lumen and transferring the other proton to an OH^- ligand of the same Mn(3) metal center.

Another distinct aspect is that the QM/MM model suggests formation of an oxyl radical during the $S_3 \rightarrow S_4$ transition and nucleophilic attack of the calcium-bound substrate water on the electrophilic oxyl radical. Formation of the oxyl radical is also suggested by Siegbahn (see Figure 13, panel b) and Messinger (see Figure 13, panel c), but the nucleophilic attack suggested by the QM/MM model is significantly different from these other proposals. Siegbahn and Messinger suggest that the oxyl radical reacts with a μ-oxo bridge, instead of reacting with a terminal calcium-bound water molecule. Brudvig (see Figure 14, panel d) and Pecoraro[24] proposed the reaction of the calcium-bound water molecule with an oxo−Mn(V) species. In contrast, the QM/MM model suggests the nucleophilic attack of an oxyl radical.

4. Conclusions

We have developed chemically sensible structural models of the OEC along the catalytic cycle of PSII with complete ligation of the 3 + 1 Mn tetramer by amino acid residues, water, hydroxide, chloride, and calcium ions. Manganese and calcium ions are ligated consistently with standard coordination chemistry assumptions, supported by much biochemical and spectroscopic data. The proposed models are found to be stable and entirely consistent with available mechanistic data as well as in good qualitative agreement with X-ray diffraction models of PSII and EXAFS measurements. The OEC structure, however, is partially undetermined since full quantitative agreement between calculated and experimental high-resolution spectroscopic data is yet to be reached. Nevertheless, the DFT QM/MM structures provide new fundamental insight that is relevant to the elucidation of the detailed mechanistic aspects of photosynthetic water splitting and the structure of the OEC.

Supporting Information Available: Comparative analysis of mechanistic models discussed in Section 3.5; complete ref 36 information; Supporting Information references. This material is available free of charge via the Internet at http://pubs.acs.org.

JA076130Q